

Supplementary Information

Deep levels in cesium lead bromide from native defects and hydrogen

Michael W. Swift

*ASEE Postdoctoral Fellow Resident at Center for Computational Materials Science,
US Naval Research Laboratory, Washington, DC 20375, USA*

John L. Lyons

Center for Computational Materials Science, US Naval Research Laboratory, Washington, DC 20375, USA

S.I. CHEMICAL POTENTIALS

Chemical potentials are variables which reflect growth conditions. Allowed values are constrained by alternative phases using a standard methodology [1,3]. CsPbBr₃ itself must be stable:

$$\mu_{\text{Cs}} + \mu_{\text{Pb}} + 3\mu_{\text{Br}} = \Delta H_f(\text{CsPbBr}_3), \quad (\text{S.1})$$

where $\Delta H_f(\text{CsPbBr}_3)$ is the formation enthalpy of CsPbBr₃. This allows one of the chemical potentials to be treated as a function of the other two, reducing the phase diagram to two degrees of freedom. We choose to eliminate μ_{Cs} , so μ_{Pb} and μ_{Br} are variables. The chemical potentials are further bounded from above by the constraint that potential precipitating phases are not stable. These include the elemental forms of the constituents (the chemical potential reference is zero, so this constraint requires $\mu_i \leq 0$) and other compounds. Cs₄PbBr₆, CsBr₃, CsBr, Cs₄Pb₉, and PbBr₂ were all tested. Excluded regions are shown shaded in Fig. S.1

Given a set of chemical potentials for Cs, Pb, and Br, the hydrogen chemical potential is found separately based on compounds formed with those elements and H. CsH was not found to be limiting under any conditions, and H forms no stable binary compounds with Pb, so μ_{H} is set to the solubility limit based on HBr: Br-rich $\mu_{\text{H}} = -0.82$ eV, balanced $\mu_{\text{H}} = -1.60$ eV, and Pb-rich $\mu_{\text{H}} = -2.38$ eV.

S.II. DEFECT FORMATION ENERGIES

Defect formation energies for all computed defects and charge states are shown in Fig. S.2 and Fig. S.3. We find that Cs_{Pb} and Pb_{Cs} form a complex, but with a binding energy of only 0.58 eV, this complex is not likely to be relevant.

Fig. S.4 shows the defect hull in balanced conditions. These results are qualitatively similar to the Pb-rich conditions from the main text. The Fermi level is somewhat lower (0.94 eV at 300 K based on all calculated defects) but the relevant set of defects is similar. The main differences are V_{Cs} and Br_{Cs} becoming more favorable (both are shallow) and H_{Br} becoming less favorable. H_i^+ is still quite favorable (0.93 eV). While Br_i^- is non-negligible (1.19 eV, see Fig. S.2) it is not part of the hull.

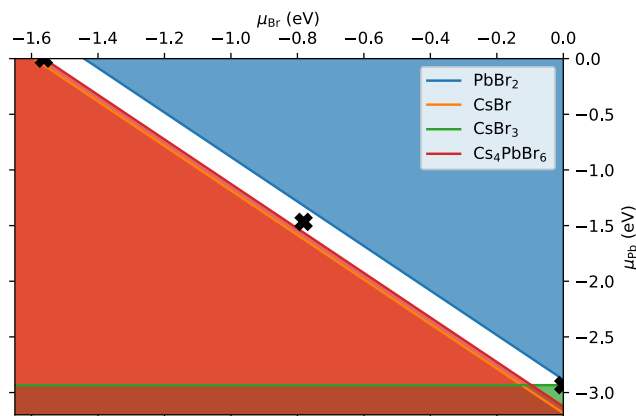


FIG. S.1. Grand canonical phase diagram for CsPbBr₃. The white region shows the values of $(\mu_{\text{Br}}, \mu_{\text{Pb}})$ for which CsPbBr₃ is stable, while shaded regions are excluded due to precipitation of alternative compounds as indicated in the legend. Three representative stable conditions are marked in black: Pb-rich ($\mu_{\text{Br}} = -1.56$ eV, $\mu_{\text{Pb}} = 0.00$ eV, $\mu_{\text{Cs}} = -2.49$ eV), balanced ($\mu_{\text{Br}} = -0.78$ eV, $\mu_{\text{Pb}} = -1.47$ eV, $\mu_{\text{Cs}} = -3.37$ eV), and Br-rich ($\mu_{\text{Br}} = 0.00$ eV, $\mu_{\text{Pb}} = -2.93$ eV, $\mu_{\text{Cs}} = -4.24$ eV). Chemical potentials are referenced to their respective elemental phases.

S.III. COMPUTATIONAL METHODS

All calculations were performed using Density Functional Theory (DFT) in the Vienna *Ab initio* Simulation Package (VASP) [4] with the projector-augmented wave (PAW) method [5] (version 54 of the PBE PAWs). Use of the standard HSE functional does not reproduce the experimental band gap of lead halide perovskites, instead leading to underestimated values. Instead, increasing the mixing parameter has been shown to reproduce experimental band gaps [6]. Here, the HSE hybrid functional [7] was used with 35% mixing and a 0.1 Å⁻¹ screening parameter in order to reproduce the experimental band gap of 2.3 eV [8]. Spin-orbit coupling (SOC) was taken into account using the non-collinear spinor method. Previous work in the perovskite MAPI [9,10] showed that both the hybrid functional and SOC are necessary to get the correct positions of defect levels within the band gap. We find the same to be true in this material.

Defect calculations used an 80-atom 2 × 2 × 1 tiling of

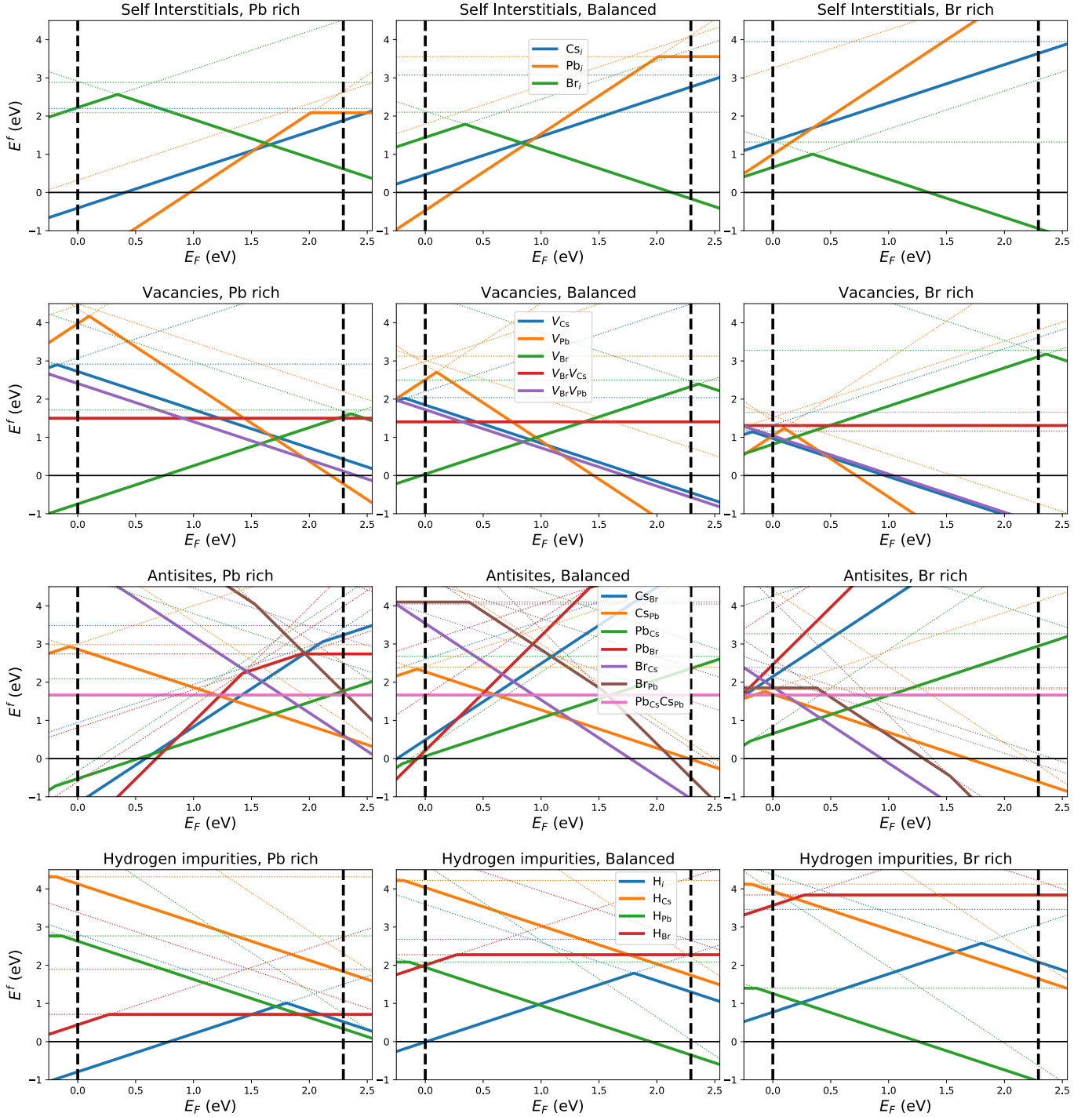


FIG. S.2. Defect formation energies (E^f) versus Fermi level (E_F) for all native defects, selected native defect complexes, and hydrogen impurities. Solid lines show favorable charge states, with kinks occurring at Fermi levels corresponding to thermodynamic charge-state transition levels. Dotted lines show higher-energy calculated charge states. The rows of plots are organized by type of defect: self interstitials, vacancies, antisites, and hydrogen impurities. Defect color-coding is shared across rows, given by legends in the middle figure. The columns show various chemical potential conditions: Pb-rich, balanced, and Br-rich (see Fig. S.1).

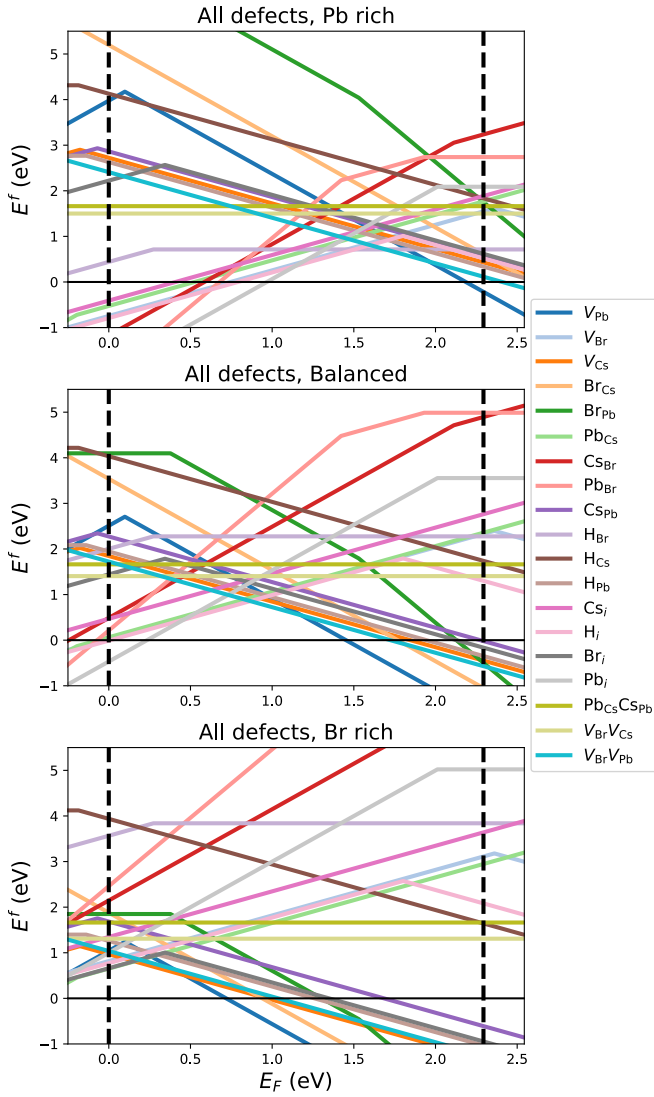


FIG. S.3. Defect lines from Fig. S.2 consolidated onto a single set of axes to aid comparison of the energies of different types of defects. The “defect hull” may be constructed from these plots by careful inspection.

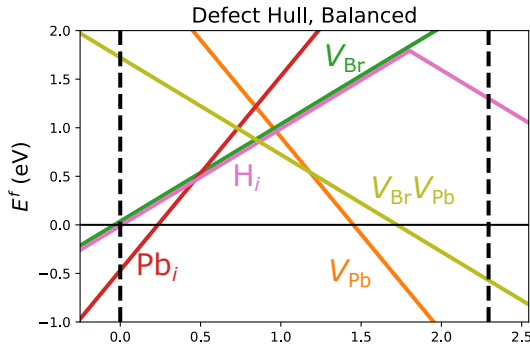


FIG. S.4. Defect formation energies (E^f) versus Fermi level (E_F) for defects that make up the “defect hull” under balanced conditions.

Pb-rich		Balanced		Br-rich	
$E_F^0 = 1.66$ eV		$E_F^0 = 0.94$ eV		$E_F^0 = 0.37$ eV	
H_{Br}^0	0.71 eV	V_{Cs}^{-1}	0.91 eV	V_{Cs}^{-1}	0.60 eV
H_i^{+1}	0.87 eV	H_i^{+1}	0.93 eV	V_{Pb}^{-2}	0.70 eV
V_{Br}^{+1}	0.92 eV	V_{Br}^{+1}	0.97 eV	H_{Pb}^{-1}	0.89 eV
H_{Pb}^{-1}	0.97 eV	Pb_{Cs}^{+1}	1.00 eV	Br_i^{-1}	0.98 eV
V_{Pb}^{-2}	1.04 eV	H_{Pb}^{-1}	1.01 eV	Pb_{Cs}^{+1}	1.02 eV
V_{Cs}^{-1}	1.06 eV	V_{Pb}^{-2}	1.03 eV	Br_i^{+1}	1.03 eV
Pb_{Cs}^{+1}	1.14 eV	Br_i^{-1}	1.19 eV	Br_{Cs}^{-2}	1.14 eV
H_i^{-1}	1.15 eV	Cs_{Pb}^{-1}	1.34 eV	H_i^{+1}	1.14 eV
Cs_{Pb}^{-1}	1.20 eV	Cs_i^{+1}	1.41 eV	V_{Cs}^0	1.16 eV
Br_i^{-1}	1.25 eV	Pb_i^{+2}	1.41 eV	V_{Br}^{+1}	1.19 eV
Cs_i^{+1}	1.25 eV	Br_{Cs}^{-2}	1.66 eV	V_{Pb}^{-1}	1.19 eV
Pb_i^{+2}	1.39 eV	V_{Cs}^0	2.04 eV	Cs_{Pb}^{-1}	1.31 eV
V_{Br}^0	1.71 eV	H_{Pb}^0	2.08 eV	Br_i^0	1.32 eV
H_{Br}^{-1}	1.72 eV	V_{Pb}^{-1}	2.09 eV	H_{Pb}^0	1.40 eV
Br_{Cs}^{-2}	1.87 eV	Br_i^0	2.10 eV	Pb_{Cs}^{+2}	1.59 eV
H_i^0	1.90 eV	Pb_{Cs}^{+2}	2.14 eV	V_{Pb}^0	1.66 eV
Pb_i^{+1}	1.99 eV	H_{Br}^0	2.28 eV	V_{Cs}^{+1}	1.69 eV
H_{Pb}^{-2}	2.00 eV	Cs_{Br}^{+2}	2.36 eV	Cs_i^{+1}	1.72 eV
Pb_i^0	2.09 eV	Br_i^{+1}	2.38 eV	Pb_i^{+2}	1.74 eV
Pb_{Cs}^0	2.09 eV	Cs_{Pb}^0	2.39 eV	Br_{Cs}^{-1}	1.77 eV
H_{Br}^{+1}	2.10 eV	V_{Br}^0	2.50 eV	V_{Pb}^{+2}	1.78 eV
Cs_{Br}^{+2}	2.16 eV	H_i^{-1}	2.66 eV	Cs_{Pb}^0	1.80 eV
Cs_i^0	2.20 eV	Pb_{Cs}^0	2.68 eV	Br_{Pb}^0	1.85 eV
Cs_{Pb}^{-2}	2.25 eV	H_i^0	2.68 eV	Br_{Pb}^{-2}	1.87 eV
V_{Br}^{-1}	2.31 eV	Pb_i^{+1}	2.73 eV	V_{Pb}^{+1}	1.89 eV

TABLE S.1. Defect formation energies of the 25 most favorable defect charge states at the charge-neutrality Fermi level E_F^0 in Pb-rich, balanced, and Br-rich conditions

the orthorhombic Pnma (62) unit cell with HSE+SOC-relaxed lattice parameters: $a = 8.21$ Å, $b = 8.39$ Å, $c = 11.74$ Å. The Brillouin zone was sampled using the special k -point $(\frac{1}{4}, \frac{1}{4}, \frac{1}{4})$. This sampling is equivalent to a $2 \times 2 \times 2$ Monkhorst-Pack grid (assuming k to $-k$ symmetry) and represents the densest possible regular sampling from a single point. Use of this special point gives converged formation energies within approximately 0.1 eV. Use of the $(\frac{1}{4}, \frac{1}{4}, \frac{1}{4})$ k -point for supercells containing charged defects has also been shown to reduce periodic image artifacts compared to Gamma-only meshes. [1] Candidate defect sites were generated using PyCDT [11], including all inequivalent sites for vacancies and antisites. Interstitial candidate sites were generated by relaxations starting from 8 inequivalent Voronoi nodes. All 123 candidate defect charge states were then screened using the PBE functional [12] with SOC. The favorable site for each defect charge state was subsequently fully relaxed with HSE+SOC until forces were less than 0.03 eV/Å. Automatically generated defect configurations were supplemented as needed by complexes, additional charge states, and configurations guided by chemical intuition. Phase

diagram analysis was partially automated using PyCDT, and processing and analysis were partially automated using pymatgen [13].

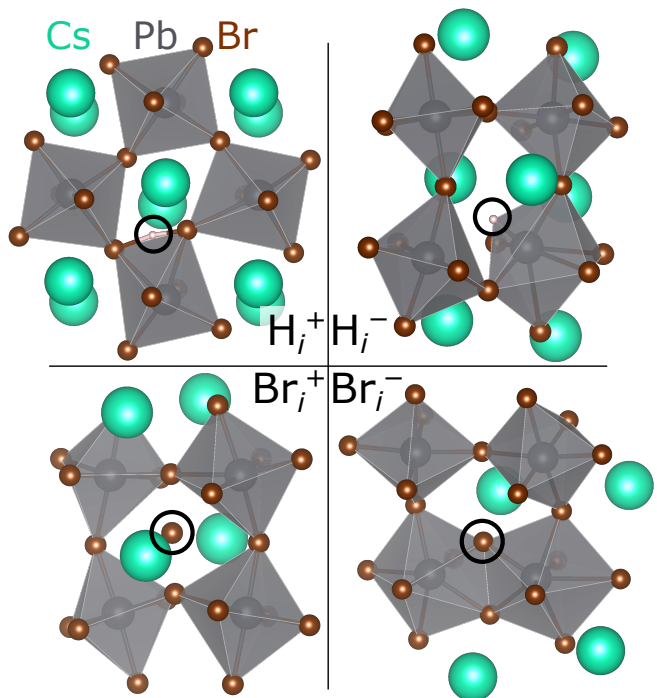


FIG. S.5. Visualization of the local structure near the hydrogen interstitial (top) and the bromine interstitial (bottom). The defects on the left are in the +1 charge state, while on the right they are in the -1 charge state. Cs are shown in green, Pb in gray, Br in brown, and H in pink.

S.IV. ATOMIC STRUCTURE OF INTERSTITIALS

The atomic structures near H_i and Br_i are shown in Fig. S.5

In its negative charge state, the bromine interstitial changes two corner-sharing squares in a $PbBr_2$ plane to edge-sharing pentagons. The distortion of the bonds is asymmetrical. The two Br atoms on the shared edge have Pb-Br bond lengths increased from 3.01 Å in the bulk to 3.25 Å and 3.22 Å to the left Pb, but 2.84 Å and 2.87 Å to the right Pb. Conversely, the Br-Pb bond opposite the shared edge are 2.93 Å to the left but 3.88 Å to the right. In its positive charge state, the bromine interstitial sits in the CsBr layer between two Cs, with a 155° Cs-Br-Cs angle, with a Br-Br distance of 2.55 Å to the bottom and 2.47 Å to the top. The Pb-Br bonds for the Br above and below the interstitial are lengthened to an average of 3.26 Å, while the opposite Pb-Br bonds are shortened to an average of 2.86 Å.

In its positive charge state, the hydrogen interstitial sits slightly off-center near an edge of a $PbBr_6$ octahedron (H-Br bond lengths of 1.57 Å and 1.86 Å), significantly shortening the Br-Br distance from 4.26 Å in the bulk to 3.48 Å, and lengthening Br-Pb bond lengths for the neighboring Br from 3.01 Å in the bulk to 3.20 Å, 3.27 Å, and 3.57 Å (from left to right in the figure). In its negative charge state, the hydrogen interstitial sits at a

face of a PbBr_6 octahedron, significantly distorting the octahedron and drawing the Pb out of the center (H–Br bond length of 1.89 Å). The further Br atoms have their bonds with Pb stretched to 3.77 Å, 3.46 Å, and 3.93 Å (from left to right in the figure).

The hydrogen interstitial configuration in this material has some similarities to its configuration in oxide perovskites such as SrTiO_3 [14], BaCeO_3 [2], and SrCeO_3 [3]. H_i^+ tends to bond with an anion, though the OH bond is shorter than the BrH bond, and the OH bond tends to point away from other atoms, as opposed to lying near a vertex of the octahedron in the perovskite. Just as in the

oxide perovskites, H_i tends to bond with a variety native defects, especially negatively charged cation vacancies. Though hydrogen is a shallow donor in SrTiO_3 and its negative charge state does not occur, the configuration of the isolated H_i^- is reminiscent of those from BaCeO_3 , SrCeO_3 , and other semiconductors [15]. The direct transition between the -1 and the $+1$ charge state (acting as a “negative- U center”) is also common [15], though in BaCeO_3 and SrCeO_3 this feature is masked by bonding with self-trapped small polarons. While small polarons have been reported in this material [16], we did not find polaron trapping associated with hydrogen impurities.

-
- [1] C. Freysoldt, B. Grabowski, T. Hickel, J. Neugebauer, G. Kresse, A. Janotti, and C. G. Van de Walle, First-principles calculations for point defects in solids, *Rev. Mod. Phys.* **86**, 253 (2014)
- [2] M. Swift, A. Janotti, and C. G. Van de Walle, Small polarons and point defects in barium cerate, *Phys. Rev. B* **92**, 214114 (2015)
- [3] M. Swift and C. G. Van de Walle, Impact of Point Defects on Proton Conduction in Strontium Cerate, *J. Phys. Chem. C* **120**, 9562 (2016)
- [4] G. Kresse and J. Furthmüller, Efficient iterative schemes for ab initio total-energy calculations using a plane-wave basis set, *Phys. Rev. B* **54**, 11169 (1996)
- [5] P. E. Blöchl, Projector Augmented-Wave Method, *Phys. Rev. B* **50**, 17953 (1994)
- [6] X. Zhang, M. E. Turiansky, and C. G. Van de Walle, Correctly Assessing Defect Tolerance in Halide Perovskites, *J. Phys. Chem. C* **124**, 6022 (2020)
- [7] J. Heyd, G. E. Scuseria, and M. Ernzerhof, Hybrid functionals based on a screened Coulomb potential, *J. Chem. Phys.* **118**, 8207 (2003)
- [8] C. C. Stoumpos, C. D. Malliakas, J. A. Peters, Z. Liu, M. Sebastian, J. Im, T. C. Chasapis, A. C. Wibowo, D. Y. Chung, A. J. Freeman, B. W. Wessels, and M. G. Kanatzidis, Crystal Growth of the Perovskite Semiconductor CsPbBr_3 : A New Material for High-Energy Radiation Detection, *Cryst. Growth Des.* **13**, 2722 (2013)
- [9] M.-H. Du, Density Functional Calculations of Native Defects in $\text{CH}_3\text{NH}_3\text{PbI}_3$: Effects of Spin–Orbit Coupling and Self-Interaction Error, *J. Phys. Chem. Lett.* **6**, 1461 (2015)
- [10] D. Meggiolaro and F. De Angelis, First-Principles Modeling of Defects in Lead Halide Perovskites: Best Practices and Open Issues, *ACS Energy Lett.* **3**, 2206 (2018)
- [11] D. Broberg, B. Medasani, N. E. Zimmermann, G. Yu, A. Canning, M. Haranczyk, M. Asta, and G. Hautier, PyCDT: A Python toolkit for modeling point defects in semiconductors and insulators, *Comput. Phys. Commun.* **226**, 165 (2018)
- [12] J. P. Perdew, K. Burke, and M. Ernzerhof, Generalized gradient approximation made simple, *Phys. Rev. Lett.* **77**, 3865 (1996)
- [13] A. Jain, G. Hautier, C. J. Moore, S. Ping Ong, C. C. Fischer, T. Mueller, K. A. Persson, and G. Ceder, A high-throughput infrastructure for density functional theory calculations, *Comput. Mater. Sci.* **50**, 2295 (2011)
- [14] J. B. Varley, A. Janotti, and C. G. Van de Walle, Hydrogenated vacancies and hidden hydrogen in SrTiO_3 , *Phys. Rev. B* **89**, 075202 (2014)
- [15] A. Janotti and C. G. Van de Walle, Hydrogen multicentre bonds, *Nat. Mater.* **6**, 44 (2007)
- [16] N. Österbacka, P. Erhart, S. Falletta, A. Pasquarello, and J. Wiktor, Small Electron Polarons in CsPbBr_3 : Competition between Electron Localization and Delocalization, *Chem. Mater.* **32**, 8393 (2020)